ELSEVIER

Ceramics International 33 (2007) 419–426

CERAMICS INTERNATIONAL

www.elsevier.com/locate/ceramint

Development of high strength hydroxyapatite by solid-state-sintering process

Sumit Pramanik [a], Avinash Kumar Agarwal [b,*], K.N. Rai [a], Ashish Garg [c]

[a] *Materials Science Programme, Indian Institute of Technology Kanpur, Kanpur 208016, India*
[b] *Department of Mechanical Engineering, Indian Institute of Technology Kanpur, Kanpur 208016, India*
[c] *Department of Materials and Metallurgical Engineering, Indian Institute of Technology Kanpur, Kanpur 208016, India*

Received 29 November 2004; received in revised form 15 September 2005; accepted 11 October 2005
Available online 27 January 2006

Abstract

Hydroxyapatite (HAp) is a potential material for various biomedical applications. In the present study, an attempt has been made to synthesize this material using simpler and cheaper method of solid-state-reaction process. Samples were prepared by mixing the ingredients and then sintering the cold compacted pellets at various temperatures from 500 to 1250 °C. X-ray diffraction, thermo-gravitometric and differential thermal analysis and Fourier transform infrared (FTIR) spectroscopy techniques were used for structural characterization of the samples. It was found that Monetite phase of hydroxyapatite forms in the unsintered powder. Upon heating up to 1250 °C, samples undergo several structural transformations with final structure being α-tri calcium phosphate (TCP) after sintering at 1250 °C. Presence of various chemical groups in the samples was analyzed using Fourier transform infrared spectrometry and the results are in accordance with the literature. Mechanical tests showed that increasing compaction pressure during cold pressing improves mechanical strength of sintered product by reducing overall porosity. Compressive, tensile and bending strength, bulk modulus (in compression), and microhardness values were found to improve after resintering the pellets at 1250 °C, which were previously sintered at the same temperature. It was also found that the mechanical properties of synthesized HAp were better as compared to the natural products. In vitro biological studies in a simulated body fluid showed around 15–20% change in the surface roughness of the samples albeit with negligible weight gain in dry state.

Keywords: A. Sintering; Hydroxyapatite; Biomaterials; Hip-joint material; Scanning electron microscopy

1. Introduction

Calcium phosphate group is the largest and the most important inorganic part of hard tissues constituting bones and dentine material in vertebrate animals. Synthetic calcium phosphate has been shown to be quite similar, crystallographically and chemically, to the natural materials in the bone [1] and has several medical applications including replacement of bony and periodontal defects, alveolar ridge, maintenance or augmentation of, spine fusion, and ear/eye implantation. Hydroxyapatite (or HAp) bioceramics as bone substitute materials have the advantages of abundant supply, low cost and absence of immunogenicity [1]. Apatite [$Ca_{10}(PO_4)_6X_2$] materials have unique biocompatibility feature among phosphate groups; X in the formula represents hydroxyl (OH^-) group for hydroxyapatite (HAp), fluoride (F^-) group for fluorapatite, chloride (Cl^-) group for chlorapatite. In particular, porous HAp implants have served as bone substitute in the clinics for long time. Porosity is required for two purposes: (a) weight reduction and (b) the ability to rapidly deliver calcium to support histological processes. HAp with controlled porosity is analogous to the natural ceramic in the bone and is bioactive in the sense that it is a non-toxic compound and interfacial bonds are able to develop between HAp and the living tissues leading to enhanced mechanical strength of the overall structure. The porosity aids in tissue growth and their binding with the HAp. However, lower mechanical strength of pure HAp has hampered its use as a bone implant material because of conflicting requirements of porosity and strength. In addition, HAp also has potential to be used in dental applications [2].

Both mechanical strength and bioactivity of HAp depend strongly upon its microstructure such as grain size and grain

* Corresponding author. Tel.: +91 512 2597982; fax: +91 512 259 7408.
E-mail address: akag@iitk.ac.in (A.K. Agarwal).

0272-8842/$32.00
doi:10.1016/j.ceramint.2005.10.025

size distribution, porosity and its shape and distribution, and material crystallinity [3]. This leaves much freedom in the hands of materials designers to improve and tailor the properties of this material depending upon the application. As a result, HAp powders have been synthesized using several methods including wet-chemical method in aqueous solutions [4], sol–gel method [5,6], hydrothermal method [6], thermal deposition [3], conversion of coastal corals [7], and continuous precipitation [8]. However, very little work has been reported on solid-state-reaction processing of HAp, a relatively simple and chemically hazard free process, which can yield large amounts of material having desirable structure and properties. Young et al. and Thamaraiselvi and Rajeswari have employed solid-state-reaction process as a part of hot isostatic processing of their samples [9,10] but the process becomes more expensive and intricate due to incorporation of hot pressing. In this paper, we present our results on the synthesis of single phase HAp using powder mixing and cold pressing, offering a simpler, faster and cheaper way of production. We have carried out detailed structural characterization using X-ray diffraction, thermal analysis, and Fourier transform infrared spectroscopy (FTIR). Mechanical properties such as compressive, tensile and bending strengths, modulus and hardness have been evaluated in detail as a function of cold compaction pressure and pore volume. Samples were also tested for their bioactivity in a simulated body fluid.

2. Materials and methods

2.1. Synthesis of hydroxyapatite (HAp)

Synthesis of HAp consists of: (a) milling of inorganic component mixture followed by compaction at pressures from 46 to 135 MPa to form a pellet, and (b) subsequently sintering at high temperatures (∼1250 °C). Typical composition of HAp contains CaO (50.52 wt.%), P_2O_5 (46.43 wt.%), SiO_2 (1.72 wt.%) and trace amounts (<1%) of other additives like alumina, hydrofluoric acid, magnesia, ferric oxide, and titania. Note that the slightly higher amount of silica than usual concentration (0.85 wt.%) was used to enhance the interfacial bonding because silica tends to form low melting compounds at the sintering temperatures used in this study [11]. Various components of HAp were taken in desired proportion to yield a HAp composition with Ca/P ratio of 1.61. Although, Ca/P ratio for stoichiometric HAp is known to be 1.67, stable HAp phase has been found to exist over a range of Ca/P ratio from 1.3 to 1.8 [12]. All the above components for synthesizing HAp are commercially available in the powder form except HF. First, the ingredients were mixed in a crucible using a mortar for 1 h. Subsequent mixing was carried out in a ball mill for 16 h in a mixed organic vehicle containing 30% (v/v) acetone and 0.2% (w/w) polyvinyl alcohol (PVA) as binder. The final mixed slurry was dried at 80 °C for 3 h, resulting into powder. This powder was pelletized using a cylindrical stainless steel dye using compaction pressures varying from 46 to 135 MPa with dwell time of 15–400 s at ambient temperature. The cold pressed HAp pellets were sintered in air in a glowbar furnace at varying temperature from 500 to 1250 °C. Sintering was carried out at a heating ramp rate of 200°/h and soaking time (1–2 h), followed by furnace cooling, used to minimize internal cracks. Final samples for property evaluation were prepared by recrushing the sintered sample followed by further compaction and sintering at 1250 °C.

2.2. Characterization

2.2.1. Structural characterization

Structural characterization of the samples was done using X-ray diffraction, differential thermal calorimetry and Fourier transform infrared spectroscopy techniques. Thermo-gravitometric analysis (TGA) and differential thermal analysis (DTA) were carried out on unsintered powder, using alumina powder as reference material on a Pyris Diamond simultaneous TG/DTA apparatus (Perkin-Elmer make, model SII) from 40 to 1300 °C in nitrogen atmosphere (flow rate 20 mL/min) [13]. Crystal structure identification of HAp samples was performed using X-ray diffraction (Seifert Diffractometer, England, model: ISO Debyeflex-2002) using Cu Kα1 radiation (λ = 1.54056 Å). Five distinct categories of samples were analyzed: (a) mixed and unsintered ground powder (sample I), samples sintered at (b) 500 °C (sample II), (c) 800 °C (sample III), (d) 1250 °C (sample IV) and (e) sample IV recrushed and sintered again at 1250 °C (sample V). These temperatures were chosen corresponding to the peaks observed in differential thermal analysis plot of unsintered powder.

The presence of chemical groups of HAp material was investigated in the spectral region 4000–400 cm^{-1} using Fourier transformation infrared spectrophotometer (Bruker make, model Vector 22). The KBr disk technique [14] was employed using few mg of HAp powder in spectroscopic–grade KBr (sample: KBr = 1:30), which was dried at 100 °C.

For morphological characterization, well polished HAp samples were studied using scanning electron microscopy (SEM) (JEOL, JSM 840A) using secondary electron mode of imaging. The Brunauer-Emmett-Teller (BET) technique was used to analyze the active surface area of crushed HAp materials using BET analyzer (Beckman Coulter make, model SA 3100), and particle size analyzer (Fritsch make, model 22).

2.2.2. Mechanical characterization

Detailed mechanical characterization was carried out to analyze the compressive, tensile and three point bending strengths of the samples using universal testing machine (UTM) (Hounsfield Test Equipment, England) at a strain rate of 0.01 mm/s. While cylindrical samples were utilized for tensile and compressive measurements, flat strips were used for bending measurements. Each measurement was made on four identical specimens. Microhardness measurements were carried out on flat and well polished samples using Vickers Microhardness Tester (Leitz, Germany) at a fixed load 4903 mN for pyramidal indentation. At least five indentations were made for obtaining an average microhardness value on each specimen.

Table 1
Typical composition of simulated body fluid (SBF)

Composition	Weight (g) per liter distilled water
Sodium chloride (NaCl)	8.2187
Potassium chloride (KCl)	0.2260
Calcium chloride ($CaCl_2 \cdot 2H_2O$)	0.3860
Sodium bi-carbonate ($NaHCO_3$)	0.3508
Di-Potassium hydrogen phosphate ($K_2HPO_4 \cdot 3H_2O$)	0.3337
Sodium sulfate deca-hydrate ($Na_2SO_4 \cdot 10H_2O$)	0.1697
Magnesium chloride hexa-hydrate ($MgCl_2 \cdot 6H_2O$)	0.3366

2.2.3. Biocompatibility in vitro test

In vitro test consisted of observing corrosive/detritus effect in HAp samples suspended in simulated body fluid (SBF) for 60 days at ambient temperature. A typical simulated body fluid composition is shown in Table 1. The degree of corrosive effect of SBF on HAp was estimated by surface roughness measurement using surface profilometer (Mitutoyo make, Model SJ 301) and by measuring the weight of the samples before and after the test.

3. Results and discussion

3.1. Structural characterization

3.1.1. X-ray diffraction

The X-ray diffraction patterns of all the samples are shown in Fig. 1. Fig. 1(a) shows the pattern for mixed and dried but unsintered powder. Most of the peaks in this pattern match with the Monetite or $CaPO_3(OH)$[*JCPD File No.* 09-0080] and calcium deficient hydroxyapatite or $Ca_9(HPO_4)(PO_4)_5OH$ [*JCPD File No.* 46-0905]. This shows that that individual powders when mixed in presence of liquid HF, are able to chemically combine together and form the hexagonal structure of HAp. We also carried out the line broadening analysis of the various peaks using Debye Scherrer equation [15] and found the crystallite size to be approximately 50–70 nm. Appropriate correction for the instrumental broadening was made during the calculation. The XRD pattern of as mixed powder (sample I) is shown in Fig. 1(a). The XRD patterns corresponding to the samples sintered at 500 (sample II), 800 (sample III), and 1250 °C (sample IV) are shown in Fig. 1(b), (c), and (d) respectively. While major peaks of XRD pattern of the sample calcined at 500 °C matches well with β-pyrophosphate or β-$Ca_2P_2O_7$ [*JCPD File No.* 09-0346], there are some peaks indicating the presence of $Ca_9(HPO_4)(PO_4)_5OH$. The pattern of sample sintered at 800 °C corresponded to the β-tricalcium phosphate or β-TCP or β-$Ca_3(PO_4)_2$ [*JCPD File No.* 09-0169] with some amounts of β-$Ca_2P_2O_7$ still present. The pattern of sample sintered at 1250 °C to α-tricalcium phosphate or α-TCP phase or α-$Ca_3(PO_4)_2$ [*JCPD File No.* 29-0359]. The major peaks of XRD pattern for sample V (obtained after recrushing the sample IV and resintering again at 1250 °C) is shown in Fig. 1(e). Most peaks of this pattern for sample V can be indexed to the β-TCP suggesting a subtle crystallographic change upon recrushing and resintering the sample. However, it must be noted that since there are very subtle differences between the crystal structure of α-TCP and β-TCP, this transition cannot be concluded with certainty. Also it is reported [16] that the presence of amorphous $Ca_2P_2O_7$ and β-$Ca_2P_2O_7$ in the samples sintered below 750 °C. However, in our samples sintered at and below 800 °C, existence of amorphous phase can be ruled out due to fairly sharp crystallinity of the peaks in the diffraction patterns. It can also be noticed from the comparison between the XRD patterns in Fig. 1(d) and (e), that the peaks in the sample V (resintered at 1250 °C) are stronger than the sample annealed only once at 1250 °C and this is mainly due to the large sintering time for this sample which leads to enhanced crystallization as well as reduction in strain and defect density. These different crystal systems of the different phases observed in our HAp samples are also supported by the literature [17–19].

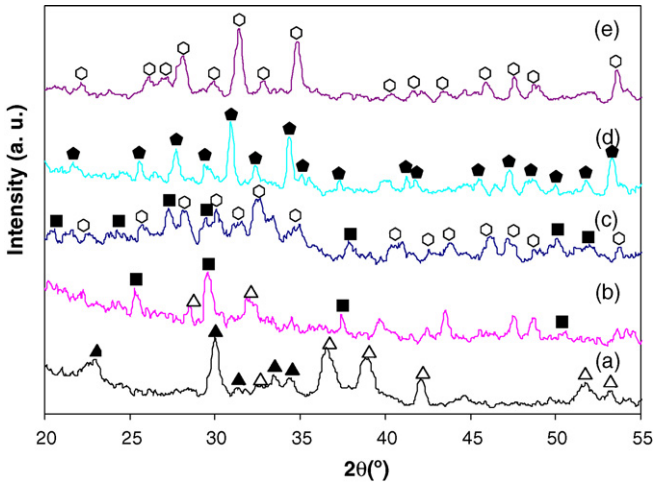

Fig. 1. X-ray diffraction pattern of HAp specimens: (a) apatite powder before first sintering; (b) apatite pellet first sintering at 500 °C; (c) apatite pellet first sintering at 800 °C; (d) HAp pelletized at 135 MPa first sintering at 1250 °C; and (e) second time sintered and recrsuhed HAp powder. The symbols indicate: $CaPO_3(OH)$ (▲) [JCPDS file No. 09-0080]; $Ca_9(HPO_4)(PO_4)_5OH$ (△) [JCPDS File No. 46-0905]; β-$Ca_2P_2O_7$ (■) [JCPDS File No. 09-0346]; α-$Ca_3(PO_4)_2$ (⬟) [JCPDS File No. 29-0359]; and β-$Ca_3(PO_4)_2$ (⬡) [JCPDS File No. 09-0169].

3.1.2. Thermal analysis

To completely understand the phase transformation in our HAp samples, we performed DTA/TGA studies and the results are shown in Fig. 2. Figure shows very little weight loss in the beginning in the TGA plot, i.e. from 40 to 200 °C which is mainly due to moisture evaporation followed by steep weight loss (∼4%) between 380 and 400 °C. This weight loss is also confirmed by sharp peaks in the DTA plot in the same temperature range. This weight loss in this region can be attributed to thermal dissociation of hydroxyl group (small peak at ∼310 °C) and chemical decomposition of acid phosphate to the pyrophosphate (large peak at ∼380 °C). This is also confirmed by the XRD plot (see Fig. 1(b)) where samples sintered at 500 °C shows pyrophosphate phase. The second region of less steeper weight loss (∼2%) lies between 550 and 650 °C approximately accompanied by a very small peak in the

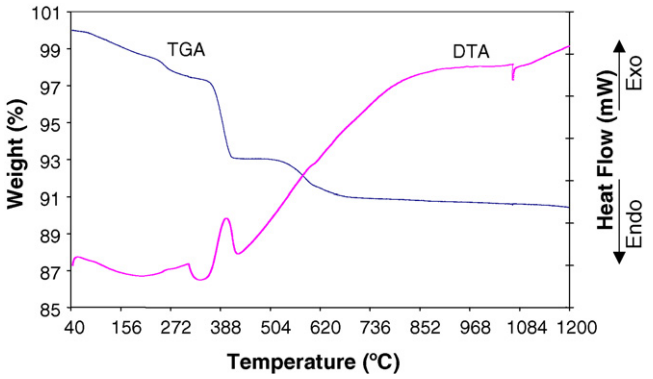

Fig. 2. TGA/DTA curves of HAp after mixing of ingredients.

DTA plot as well. The weight loss in this region can be attributed to the structural transformation of orthophosphate to β-$Ca_2P_2O_7$. This is again corroborated by XRD pattern (Fig. 1(c)) where sample sintered at 800 °C shows the presence of β-$Ca_3(PO_4)_2$ phase. Beyond 750 °C, weight loss is insignificant and there is a sharp DTA peak at around 1063 °C, which can be attributed to the phase transformation from β-$Ca_3(PO_4)_2$ to α-$Ca_3(PO_4)_2$, again evident from the XRD pattern of sample sintered at 1250 °C (see Fig. 1(d)).

3.1.3. FTIR measurements

The FTIR spectra of unsintered hydroxyapatite, i.e. sample I and the sample V (resintered at 1250 °C) are shown in Fig. 3. The peaks in the spectra and their association to respective chemical groups are summarized in Table 2. These assignments to specific chemical groups are in agreement with the observation of other groups [17,19].

In the spectra of unsintered HAp, the broad band at about 3400 cm^{-1} corresponds to the absorbed hydrate and the sharp peak between 3570 and 3670 cm^{-1} belongs to the stretching vibration of lattice OH^- ions [20]. Both these peaks are not seen in the sample V indicating the disappearance of the hydrated groups and structural change. There are several other small peaks between 400 and 1900 cm^{-1} which are representative of P–O–H and HPO_4^{2-} groups and these peaks disappear upon sintering the sample at 1250 °C [17,21]. The characteristic peak of PO_4^{3-} appear at 1090, 1040–1014, 950–937, 601–597, 570–558 and 470–420 cm^{-1} and these peaks remain in the sintered sample as well since it is the core group of α-TCP also.

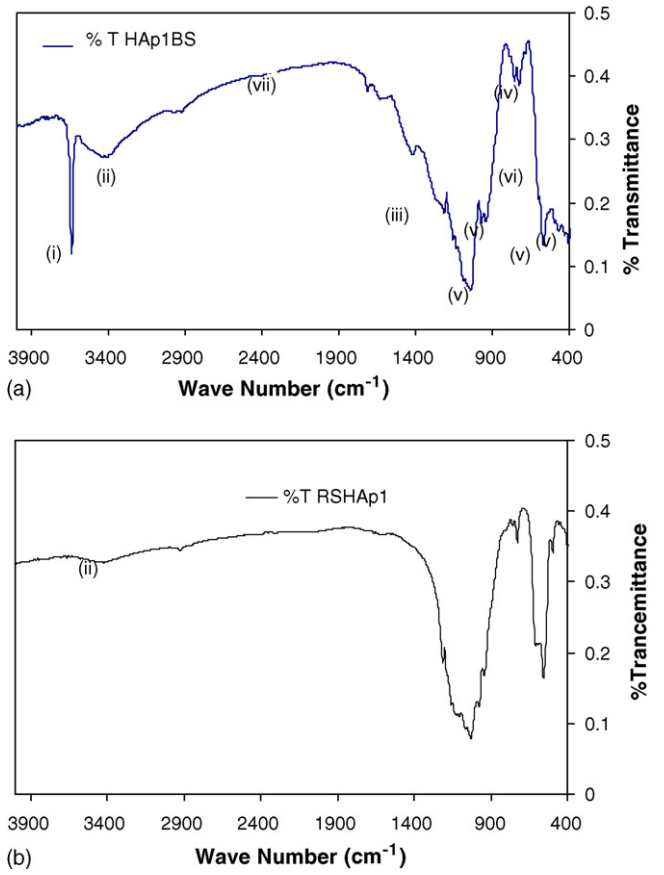

Fig. 3. FTIR spectrograph for (a) HAp before sintering; (b) crushed and sintered (1250 °C) HAp.

3.1.4. Morphology study

Scanning electron images of the sample sintered at 1250 °C (sample IV) and sample V (resintered at 1250 °C) are shown in Fig. 4. It can be seen that recrushed and resintered HAp materials exhibit a well connected grain structure with an average grain size of approximately 7–8 μm. No significant grain growth was observed in the resintered sample. The white particles observed in Fig. 4(a) are unreacted CaO particles, which transform almost completely in sample V (after recrushing and resintering). Surface porosity was visible in both samples. Bulk density in these samples varied from 1.8 to 2.5 g/cm^3 as measured by image analysis (by measuring the area fraction of the pores on the surface) and also by using

Table 2
List of chemical groups belonging to peaks in FTIR spectra for samples I and V

Sample	Peak in spectra	Wave number (cm^{-1})	Chemical bonding for HAp before sintering
Sample I: HAp before sintering	(i)	3670–3570	Sharp peak for stretching vibration OH^- ion
Sample V: HAp before sintering and after sintering at 1250 °C	(ii)	3500–3100	Hydrated O–H
	(iii)	1250	HPO_4^{2-} Weak shoulder for P–O–H in plane
	(iv)	760–720	Weak peak out-of-plane
	(v)	1090, 1040–1014, 950–937, 601–597, 570–558, and 470–420	PO_4^{3-}
	(vi)	635–628	Medium sharp peak for O–H bending deformation mode
	(vii)	2349	Weak peak for KBr absorption

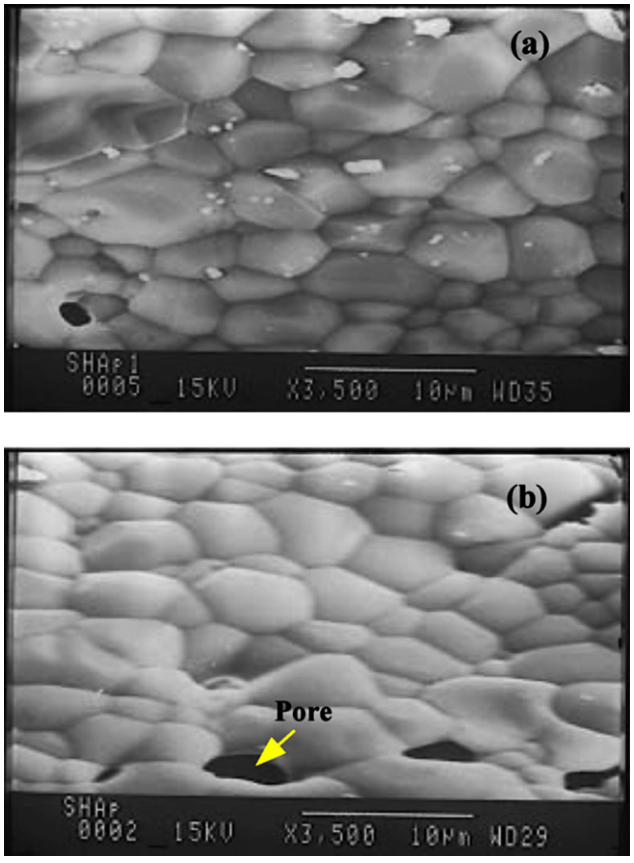

Fig. 4. SEM micrographs of (a) sintered HAp (compacted at 135 MPa and sintered at 1250 °C for 1 h) and (b) recrushed and second time sintered HAp (compacted at 135 MPa, sintered at 1250 °C for 1 h).

Archimedes principle. A comparison with theoretical density [22] (3.16 g/cm^3) gives the maximum gross porosity to be approximately 42%.

3.2. Mechanical characterization

We measured three different mechanical properties of our samples, viz. tensile, compressive and bending strengths, three important parameters defining suitability of HAp for biomedical applications. Fig. 5 shows the results of compression, 3-point bending and tension tests performed on sample V (recrushed and resintered) which was cold compacted at a pressure of 135 MPa. The fracture stress in compression was found to be ∼270 MPa at a strain of ∼0.027 whereas tensile fracture stress was approximately 120 MPa with fracture strain of ∼0.15. In 3-point bending tests, samples exhibited a fracture stress of 55 MPa at a fracture of 0.016. These values are significantly higher than those reported in literature [23]. It can be expected for the samples to show higher compressive strength than tensile because surface cracks open in tension and close in compression. Unlike behaviour of normal ceramics, HAp samples in present investigation exhibit two distinct regions of deformation: an initially linear region (Region I) followed by a steeper linear region (Region II) where stress increases very fast until the onset of fracture. The region-I extends up to ∼1% strain for compressive and bending mode and ∼10% strain for

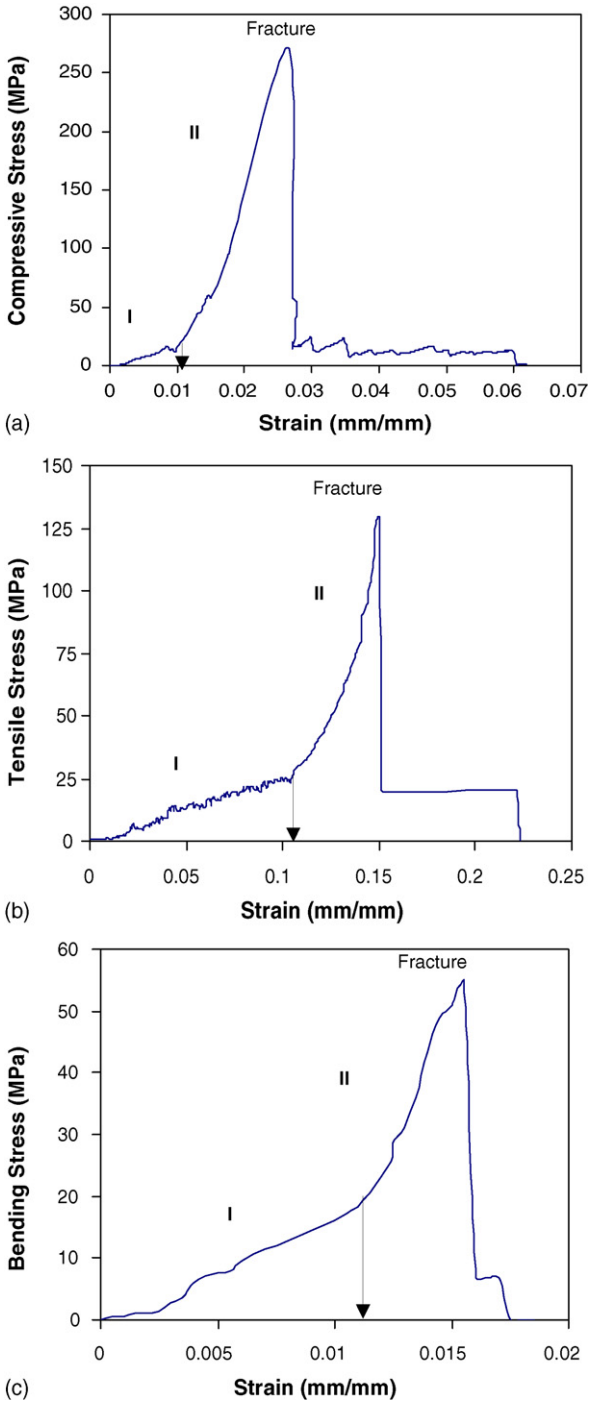

Fig. 5. (a) Compressive, (b) tensile, and (c) bending stress-strain plots for recrushed and second time sintered (at 1250 °C) HAp sample compacted at 135 MPa.

tensile mode and is depicted by very slow increase of stress whereas very fast steeper increase of stress is observed in region-II until the onset of fracture. Region-II depicts mechanical behaviour of typical ceramic whereas region-I is due to closing of pores in the initial stages of deformation test since samples contain very high (∼40%) but not interconnected porosity.

We also measured the Young's modulus of sample V in compression and measured its variation with the cold

Table 3
Young's modulus in compression, fracture strength in compression, tensile, and bending with various cold compaction pressures (with a constant strain rate of 0.01 mm/s) for HAp materials after second time sintering at 1250 °C[a]

CCP (MPa)	E_C (GPa)	CS (MPa)	TS (MPa)	BS (MPa)
46	1.821 ± 0.16	21.317	–	7.68
60	4.463 ± 0.39	34.116	–	–
75	9.405 ± 0.92	63.258	–	–
90	11.663 ± 1.05	95.027	18	26.4
105	12.048 ± 1.18	131.491	–	–
120	15.954 ± 1.61	188.132	–	–
135	20.23 ± 2.12	271.161 ± 4.95	129.65	54.5

[a] CCP: cold compaction pressure; E_C: bulk modulus in compression; CS: compressive strength; TS: tensile strength; BS: three point bending strength or flexural strength.

compaction pressure during pelletization. It was found that as the cold compaction pressure increases, both compressive strength and modulus increase as shown in Table 3 and Fig. 6. This is due to decrease in the pore volume in the sample which also decreases upon increasing the cold compression pressure as shown in Fig. 7. The samples fabricated at a compaction pressure of 135 MPa show the modulus of ~20 GPa and compressive strength of the order of ~270 MPa. Increase in cold compaction pressure is also found to increase the fracture strength of sintered product as shown in Fig. 6. The variation of specific surface area and specific pore volume of the particles with cold compaction pressure and both strength and modulus in compression varies with specific pore volume for HAp materials after second time sintering at 1250 °C as shown in Table 4.

To investigate above results in detail, active surface area and pore volume of HAp material were studied as a function of cold compaction pressure and these were related to the compressive strength and modulus of the sample V. The variation of specific internal surface area (SA) and pore volume (V_p) of the sample V with cold compaction pressure is shown in Fig. 7, exhibiting a

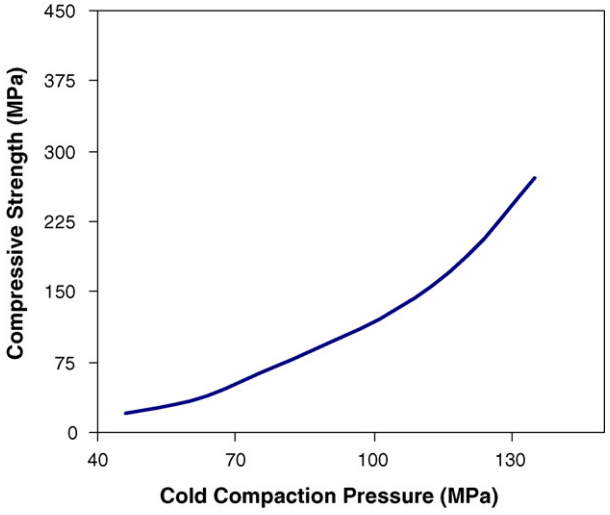

Fig. 6. Variation of maximum compressive strength (CS) or fracture strength with increasing cold compaction pressure (CCP) for recrushed and second time sintered HAp material.

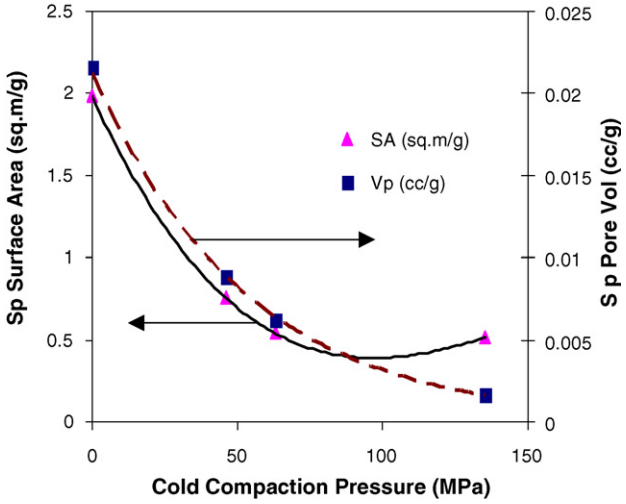

Fig. 7. Variation of specific pore volume and specific particle surface area for recrushed and second time sintered HAp with cold compaction pressure.

decreasing trend with increasing cold compaction pressure (P_{CCP}). This can also be analyzed using following relations.

$$SA = -6 \times 10^{-07}[P_{CCP}]^3 + 0.0003[P_{CCP}]^2 - 0.0387[P_{CCP}] + 1.981 \quad (1)$$

$$V_p = 0.0213.\exp\{(-0.019)[P_{CCP}]\} \quad (2)$$

The mechanical properties like compressive fracture strength and Young's modulus also decreased with increasing pore volume of the samples, which is shown in Fig. 8.

We also conducted microhardness measurements on our samples. Vickers microhardness of HAp was found to improve marginally with second time sintering (sample V) as shown in Table 5. Average hardness of freshly produced sintered HAp materials is 5.272 GPa (537.5 kgf/mm^2) which is similar to the values reported in the literature [24,25]. However, both of these values are significantly higher than the values obtained on both, cancellous and cortical bone as measured in our laboratory. The hardness of sample V was found to be almost 15–16 times better than natural femoral bone. This difference is related to the calcium content of the two bone types [26]. In addition, this may also result from large intra-granular porosity/cavitation in first time sintered products (sample IV) which is reduced when samples are resintered (sample V).

Table 4
Variation of particles specific surface area, specific pore volume, compressive strength, and bulk modulus (compression) with cold compaction pressure for HAp sample V (resintered at 1250 °C)

CCP (MPa)	Specific pore volume (cm^3/g)	Specific SA (m^2/g)	CS (MPa)	E_C (GPa)
0	0.02164	1.981	0.00	0.000
46	0.00881	0.755	21.317	1.821
63	0.00623	0.54	34.116	4.463
135	0.00165	0.513	271.161	20.23

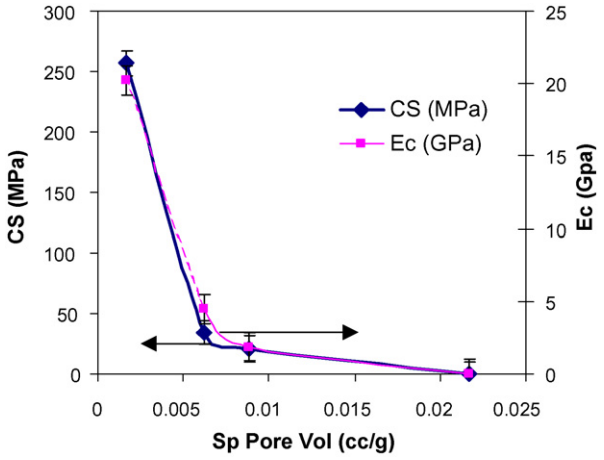

Fig. 8. Dependence of compressive strength (MPa) and Young's modulus (GPa) on specific pore volume (cm^3/g).

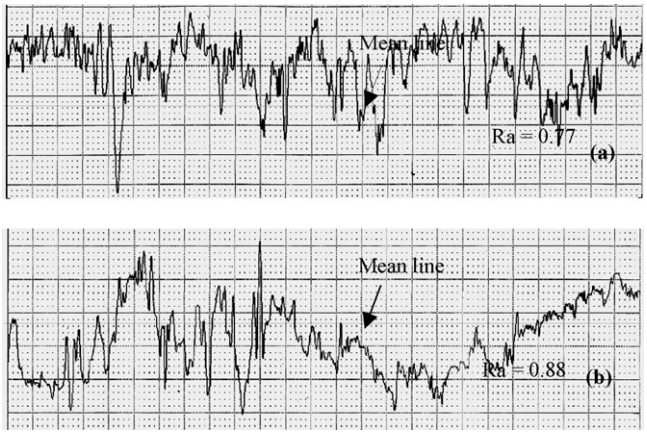

Fig. 9. Surface profile of polished recrushed and second time sintered HAp (a) before immersion into the SBF; (b) after immersion in SBF (Scale: vertical—2.0 μm/cm, horizontal—200.0 μm/cm, traverse length 2.5 mm).

Table 5
Comparison of Vickers microhardness of HAp materials and bone (as measured)

Material	Average Vickers hardness (GPa)	Average Vickers hardness (kgf/mm^2)
First time sintered hydroxyapatite	5.272 ± 0.448	537.5 ± 45.67
Recrushed and sintered hydroxyapatite (RSHAp135)	5.371 ± 0.527	547.6 ± 53.72
Cortical bone	0.396 ± 0.0035	40.4 ± 0.36
Cancellous bone	0.345 ± 0.0042	35.2 ± 0.43

3.3. Biocompatibility (in vitro) study

Resistance of a biomaterial to surface dissolution in a simulated body fluid can be used as one of the parameters of biocompatibility. The roughness profile of well polished surface (R_a = 0.77 μm in Fig. 9(a)) was compared with surface profile (R_a = 0.88 μm in Fig. 9(b)) of the same surface after immersing in SBF for 60 days at 37 °C. The change in surface roughness is about +14% (ΔR_a = 0.11 μm)) after interaction of the HAp surface with SBF which could be due to some overgrowth on the sample surface. We also measured the change in the weight of the samples after immersing for 60 days in SBF which was found negligible (∼ 0.2%) in the dry state. The values of roughness and weight are also given in Table 6 for further clarification. Biological studies are under further investigation to explore these aspects and the emphasis is towards conducting in vivo tests of the samples.

4. Conclusions

We have synthesized single phase hydroxyapatite by low cost solid-state-sintering method. The material shows structural phase transitions at temperature at around 380, 600, and 1063 °C as shown by DTA/TGA analysis and confirmed by XRD. The sample sintered at 1250 °C showed the presence of α-TCP phase. FTIR results showed that the chemical groups present in our samples match well with those presented in literature. Mechanical properties such as compressive strength, tensile strength, bending strength, and Young's modulus in compression increase with an increase in cold compaction pressure during pelletization. This arises due to enhancement in the density of the samples upon increasing the cold compaction pressure. Mechanical properties of our samples were found better than those reported in the literature. Samples crushed and resintered at 1250 °C show significant improvement in the mechanical properties and good biocompatibility. Density (1.98 g/cm^3) of our HAp samples is found to be lower than conventional ceramic materials and it is close to natural bone density (1.6–2.0 g/cm^3). The surface hardness of the samples was found to be 15–16 times larger than natural femoral bone and no appreciable change in the sample weight (dry state) was found after immersing the sample in simulated body fluid for 60 days.

Table 6
Surface roughness parameters before and after immersion into the SBF

Observations		Before immersion	After 60 days immersion in SBF	% Change
Roughness parameters (μ)	Ra	0.77	0.88	+14
	Ry	6.08	5.19	+17
	Rz	4.61	5.19	+9.5
	Rq	0.98	1.06	+8.2
Weight (g)	Hexagonal prism shaped sample	0.7942 (Dry)	0.9656 (Wet)	+21.5
			0.7965 (Dry)	+0.29
	Trigonal prism shaped sample	0.6208 (Dry)	0.6779 (Wet)	+9.2
			0.6225 (Dry)	+0.27

References

[1] F.C.M. Driessens, Probable phase composition of the mineral in bone, Zeitschrift fur Naturforschung C-A, J. Biosci. 35 (5–6) (1980) 357–362.

[2] B.D. Ratner, A.S. Hoffman, F.J. Schoen, J.E. Lemons, Biomaterials Science, Academic Press, San Diego, CA, 1996.

[3] D. Shi, G. Jaing, X. Wen, in: K. Khor, et al. (Eds.), In vitro behavior of hydroxyapatite prepared by a thermal deposition method, processing and fabrication of advanced materials VIII, World Scientific, Singapore, 2001, p. 117.

[4] N. Kivrak, A.C. Tas, Synthesis of calcium hydroxyapatite-tricalcium phosphate composite bioceramic powders and their sintering behavior, J. Am. Ceram. Soc. 81 (9) (1998) 2245–2252.

[5] A. Balamurugan, S. Kannan, S. Rajeswari, Bioactive sol–gel hydroxyapatite surface for biomedical application—in vitro study, Trends Biomater. Artif. Organs 16 (1) (2002) 18–20.

[6] P. Layrolle, A. Ito, T. Tateishi, Sol–gel synthesis of amorphous calcium phosphate and sintering into microporous hydroxyapatite bioceramics, J. Am. Ceram. Soc. 81 (6) (1998) 1421–1428.

[7] M. Sivakumar, T.S.S. Kumar, K.L. Shantha, K.P. Rao, Development of hydroxyapatite derived from Indian coral, Biomaterials 17 (1996) 1709.

[8] D. Tadic, M. Epple, Mechanically stable implants of synthetic bone mineral by cold isostatic pressing, Biomaterials 24 (2003) 4565–4571.

[9] R.A. Young, D.W. Holcomb, Variability of hydroxyapatite preparations, Calcified Tissue Int. 34 (1982) 17–32.

[10] T.V. Thamaraiselvi, S. Rajeswari, Biological evaluation of bioceramic materials—a review, Trends Biomater. Artif. Organs 18 (1) (2004) 9–17.

[11] F. Singer, S.S. Singer, The Raw Materials, Industrial Ceramics, Chapman & Hall Ltd., London, 1963, pp. 108–109.

[12] E.C. Victoria, F.D. Gnanam, Synthesis and characterisation of biphasic calcium phosphate, Trends Biomater. Artif. Organs 16 (1) (2002) 12–14.

[13] C. Duval, Inorganic Thermo-gravimetric Analysis, second and revised edition, Elsevier Publishing Company, 1963.

[14] W.O. George, P.S. Mcintyre, in: D.J. Mowthorpe (Ed.), Infrared Spectroscopy: Analytical Chemistry by Open Learning, John Wiley & Sons Publisher, 1987.

[15] B.D. Cullity, Elements of X-ray diffraction, second ed., Addison Wesley, USA, 1976.

[16] D. Guo, K. Xu, Y. Han, Influence of cooling modes on purity of solid-state synthesized tetracalcium phosphate, Mater. Sci. Eng.-B 116 (2005) 175–181.

[17] G.C. Koumoulidis, T.C. Vaimakis, A.T. Sdoukos, Preparation of hydroxyapatite lathlike particles using high-speed dispersing equipment, J. Am. Ceram. Soc. 84 (6) (2001) 1203–1208.

[18] L. Calderin, M.J. Stott, A. Rubio, Electronic and crystallographic structure of apatites, Phys. Rev. B67 (2003) 134106.

[19] K. Yamashita, T. Kanazawa, in: T. Kanazawa (Ed.), Hydroxyapatite Inorganic Phosphate Materials, Materials Science Monograph, vol. 52, Elsevier, Tokyo, Japan, 1989, p. 30.

[20] K.C. Blakeslee, R.A. Condrate, Vibration spectra of hydrothermal prepared hydroxyapatite, J. Am. Ceram. Soc. 54 (1971) 559–563.

[21] K. Nakamoto, Infrared and Raman Spectra of Inorganic and Coordination Compound, fourth ed., Wiley-Interscience Publication, USA, 1986.

[22] M. Komath, H.K. Varma, R. Sivakumar, On the development of an apatitic calcium phosphate bone cement, Bull. Mater. Sci. 23 (2) (2000) 135–140.

[23] E. Charrière, S. Terrazzoni, C. Pittet, P. Mordasini, M. Dutoit, J. Lemaître, P. Zysset, Mechanical characterization of brushite and hydroxyapatite cements, Biomaterials 22 (2001) 2937–2945.

[24] S. Ramesh, Grain size—properties correlation in polycrystalline hydroxyapatite bioceramic, Malays. J. Chem. 3 (1) (2000) 0035–0040.

[25] W. Suchanek, M. Yashima, M. Kakihana, M. Yoshimura, Processing and mechanical properties of hydroxyapatite reinforced with hydroxyabatite whiskers, Biomaterials 17 (1996) 1715–1723.

[26] R.H.C. Bonser, Longitudinal variation in mechanical competence of bone along the Avian Humerus, J. Exp. Biol. 198 (1995) 209–212.